Visualizing *ex vivo* radiofrequency and microwave ablation zones using electrode vibration elastography

Ryan J. DeWall[a)] and Tomy Varghese[a)]
Department of Medical Physics, University of Wisconsin-Madison, Madison, Wisconsin 53705 and Department of Biomedical Engineering, University of Wisconsin-Madison, Madison, Wisconsin 53705

Chris L. Brace
Department of Biomedical Engineering, University of Wisconsin-Madison, Madison, Wisconsin 53705

Purpose: Electrode vibration elastography is a new shear wave imaging technique that can be used to visualize thermal ablation zones. Prior work has shown the ability of electrode vibration elastography to delineate radiofrequency ablations; however, there has been no previous study of delineation of microwave ablations or radiological–pathological correlations using multiple observers.
Methods: Radiofrequency and microwave ablations were formed in *ex vivo* bovine liver tissue. Their visualization was compared on shear wave velocity and maximum displacement images. Ablation dimensions were compared to gross pathology. Elastographic imaging and gross pathology overlap and interobserver variability were quantified using similarity measures.
Results: Elastographic imaging correlated with gross pathology. Correlation of area estimates was better in radiofrequency than in microwave ablations, with Pearson coefficients of 0.79 and 0.54 on shear wave velocity images and 0.90 and 0.70 on maximum displacement images for radiofrequency and microwave ablations, respectively. The absolute relative difference in area between elastographic imaging and gross pathology was 18.9% and 22.9% on shear wave velocity images and 16.0% and 23.1% on maximum displacement images for radiofrequency and microwave ablations, respectively.
Conclusions: Statistically significant radiological–pathological correlation was observed in this study, but correlation coefficients were lower than other modulus imaging techniques, most notably in microwave ablations. Observers provided similar delineations for most thermal ablations. These results suggest that electrode vibration elastography is capable of imaging thermal ablations, but refinement of the technique may be necessary before it can be used to monitor thermal ablation procedures clinically. © *2012 American Association of Physicists in Medicine.*
[http://dx.doi.org/10.1118/1.4758061]

I. INTRODUCTION

There is an increasing shift in cancer treatment towards minimally invasive procedures. In the liver, for example, small hepatic tumors have historically been removed via surgical resection, which is inherently invasive and not indicated for up to 80% of patients.[1,2] New treatment procedures, such as radiofrequency (RF) and microwave (MW) ablation, offer a minimally invasive alternative for some primary and secondary cancers.[3–5] After initial success in the liver, thermal ablation is now routinely used to treat tumors in the kidney,[6,7] lung,[8,9] and bone.[10]

Reliable imaging feedback is essential to monitor the treatment to ensure complete tumor destruction after any ablation procedure. Thermal ablations must encompass the entire tumor, as well as a surrounding safety margin of 4–10 mm. If this is not achieved, tumor recurrence is more likely.[11] Unfortunately, studies have shown ambiguity in differentiating ablated, untreated malignant, and untreated normal tissue when monitoring thermal ablation procedures with ultrasound, computed tomography (CT), or magnetic resonance imaging (MRI).[12,13] Traditional ultrasound is typically used

to guide the ablation needle into the pathological target[13] but is a poor predictor of ablation extent during the ablation procedure.[14] Following treatment, the ablation zone does not exhibit consistent echogenic properties.[15] CT is capable of delineating thermal ablations within 2–3 mm; however, this is less applicable in real-time, and there are concerns with exposing the patient to ionizing radiation. MRI offers performance similar to CT, but scanners are often not readily available, and special MRI-compatible thermal ablation needles are required.[13] Developing new imaging modalities is essential to improving existing thermal ablation treatments, as well as extending ablation therapy to new applications.

Several ultrasound elastography modalities, techniques that image tissue stiffness, may hold promise in monitoring thermal ablation therapies. Tissue heating during ablation procedures leads to protein denaturation and tissue desiccation, increasing the Young's Modulus (i.e., stiffness) of the tissue.[16] In addition, many cancers exhibit increased stiffness with respect to the surrounding background.[17,18] Sonoelastography has been used to delineate high-intensity focused ultrasound (HIFU) and RF ablations *ex vivo*.[19] Electrode displacement elastography has shown good inclusion delineation

in phantoms, *ex vivo* liver RF ablations, and *in vivo* RF ablations.[20–22] Acoustic radiation force imaging (ARFI) has been used to image preablation malignancies and postablation thermal lesions.[23]

Techniques that estimate the Young's Modulus may provide a more direct measure of tissue stiffness. Good ablation zone visualization has been demonstrated *in vivo* by reconstructing the relative elastic modulus from RF ablation strain fields.[24] Supersonic shear imaging (SSI) has shown success delineating HIFU ablations in muscle and liver tissue at shallow depths (<30 mm).[25, 26] Mechanical needle vibration is useful for generating shear waves deeper in tissue.[27] Electrode vibration elastography (EVE), a recently developed technique, uses transient needle vibration to estimate shear wave velocity of the treated tissue formed around a RF electrode or MW antenna.[28]

EVE shows promise, as it uses a mechanical vibration source, i.e., the ablation electrode or antenna that is already being utilized during the clinical procedure. However, an extensive investigation of the feasibility of visualizing thermal ablation zones with this technique has not been conducted. A comprehensive study is necessary to evaluate how effectively EVE portrays the ablation zone. Additionally, previous studies have primarily focused on visualizing RF ablations. MW ablation is an emerging thermal ablation technique that is capable of generating greater temperatures and larger desiccation zones in tissue,[29] which may influence stiffness distribution. In this study, we investigate radiological–pathological correlations in RF and MW ablations on shear wave velocity images, maximum displacement images, and a combination of the two viewed concurrently to gain a better understanding of how shear wave imaging portrays the ablation zone.

II. MATERIALS AND METHODS

II.A. *Ex vivo* experiments

Thermal ablations were formed in fresh *ex vivo* bovine liver tissue obtained from a local slaughterhouse. Bovine liver tissue was roughly cut into 8 cm cubes, which were placed into acrylic boxes. Molten beef hide gelatin was poured around the tissue cubes. Thirteen RF ablations were formed in liver samples from different animals using a Cool-tip[TM] RF ablation system (Valleylab; Boulder, CO) and a 1.5 mm (17 gauge) RF electrode with 2 cm active length. The electrode was inserted approximately 5 cm into the liver, and power was applied for one to three minutes using the RF generator's impedance-controlled power pulsing algorithm to form ablations ranging in size from roughly 15 mm × 15 mm × 25 mm to 25 mm × 25 mm × 35 mm. Additionally, 14 MW ablations were formed in liver samples from different animals using a 2.45 GHz MW generator and prototype dual-slot MW antenna approximately 2.2 mm in diameter (14 gauge). The power was set to 45 W and applied for 1–3 min to form ablations similar to those created using the RF generator. All ablations were imaged within 10 min of ablation formation using traditional B-mode imaging and EVE.[28] Following data acquisition, fiducial markers were inserted into the imaging

plane on both sides of the transducer, and the ablation was sliced through this plane and photographed.

II.B. Electrode vibration elastography

EVE was performed as previously described.[28] Shear waves were generated using a piezoelectric actuator (Physik Instrumente (PI) GmbH & Co. KG, Karlsruhe, DE) that was attached to the RF electrode or MW antenna. The thermal ablation needle was transiently vibrated with a 100 μm amplitude Gaussian-shaped perturbation 10 ms in duration in the positive z direction (i.e., towards the transducer), and the shear wave generated by the needle motion was tracked using an Ultrasonix SonixTOUCH scanner and L14-5/38 transducer (Ultrasonix Medical Corporation; Richmond, BC, Canada).

High frame rates are needed to track shear wave motion through the transducer's field of view. Frame rates on the order of 1000–5000 Hz have been accomplished with plane wave insonification.[30] However, our scanner did not have this capability. In order to get the high frame rates necessary for shear wave tracking, we sequentially scanned five adjacent locations on the transducer for a single perturbation to track shear wave motion, similar to the methods employed by Palmeri *et al.*[31] See DeWall *et al.*[28] for a diagram of the firing sequence. Following a perturbation and tracking sequence, the needle was perturbed again, and the adjacent five locations were tracked. This process was repeated across the face of the transducer.

II.C. Shear wave velocity reconstruction

Shear wave velocity was reconstructed using the time-to-peak algorithm.[31] Displacements were estimated using one-dimensional cross correlation on the radiofrequency data acquired during the thermal needle vibration to track shear wave propagation through the ablation and into the untreated background. The time-to-peak displacement was estimated and used to estimate shear wave velocity.[31] We assumed bidirectional wave propagation,[32] i.e., both axial and lateral gradients were estimated using a five point least-squares fit, and both gradient images were compared on a pixel-by-pixel basis. The larger of the two gradients was the assumed wave propagation direction and was used in a combined gradient image. Taking the inverse of the combined gradient image yielded the shear wave velocity image. Additionally, a maximum displacement image was generated, which represented the maximum displacement of the shear wave at each pixel location.

II.D. Measurement of thermal ablation zone

Thermal ablation zones were manually segmented on elastographic and gross pathology images. Three independent observers delineated the RF and MW ablations on shear wave velocity and maximum displacement images using ImageJ (Wayne Rasband; National Institutes of Health). Shear wave velocity and maximum displacement images were also used simultaneously to delineate the ablation using the ImageJ Sync_Win plugin to evaluate whether using information from

both images provided more accurate ablation delineation. Gross pathology was delineated by visual inspection of an image of the ablation slice by consensus of all observers to provide a "ground truth" ablation representation. Observers looked for the sharp transition in tissue color that occurs at the boundary between ablated and untreated tissue. All three observers were biomedical engineers who are active in thermal ablation research.

Gross pathology images were registered to elastographic imaging following delineation by maximizing the similarity between the two segmented regions. First, the centroids of the elastographic image mask and gross pathology mask were estimated and aligned. Following this, the gross pathology mask was rotated and translated in the x and y directions until the similarity between the two images was maximized. Finally, the registered gross pathology image and image mask were saved for comparison with elastographic imaging, as described below.

The observers completed manual segmentation of elastographic images using the following instructions. First, the observers were instructed to delineate RF and MW ablations using shear wave velocity images, based on high shear wave velocity contrast. Previously described examples of artifacts that may occur above and below the ablation or near blood vessels within the ablation were also provided.[28] Second, the observers were instructed to delineate the ablation from maximum displacement images, which were randomized when compared to the shear wave velocity images. The instructions stated that a 100 μm perturbation motion was used. Third, the observers were given corresponding pairs of shear wave velocity and maximum displacement images, and a single delineation was made using both images. The images were synced using the Sync_Win plugin in ImageJ. The boundary trace appeared on both images and was adjusted until the observer felt that it best represented the combination of the information contained in both images.

Image masks were saved for further analysis. The ablation area was estimated using the ImageJ polygon tool, and the short and long axes were visually estimated using the straight line tool, passing the line through the centroid of the elliptically shaped ablation. The correlation between elastographic imaging and gross pathology dimensions was quantified using the Pearson coefficient.

Radiological-pathological overlap and interobserver variability were quantified on shear wave velocity, maximum displacement, or combined shear wave velocity and maximum displacement segmentations. The overlap, or Jaccard index, is

$$J(A, B) = \frac{A \cap B}{A \cup B}, \tag{1}$$

where A and B are the imaging modality area and pathology delineations of a particular observer, respectively. The observer overlap was calculated for all image sets as

$$J(X, Y, Z) = \frac{X \cap Y \cap Z}{X \cup Y \cup Z}, \tag{2}$$

where X, Y, and Z represent the segmentations of all three observers on a given modality image (e.g., segmentations of all
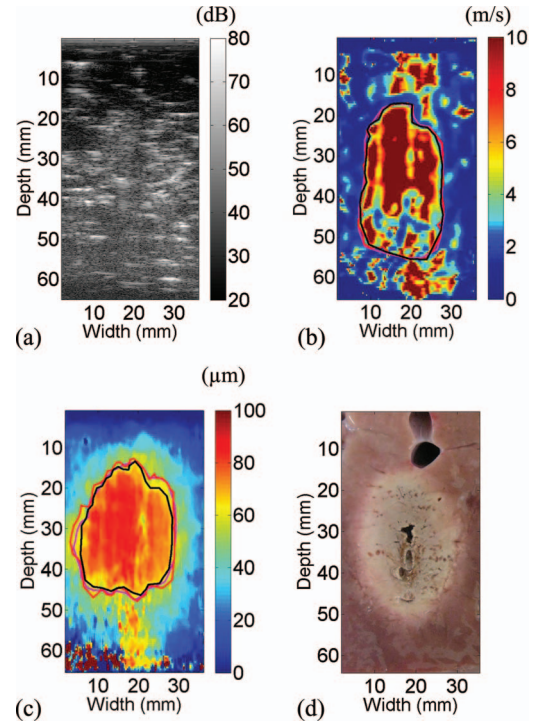

FIG. 1. Representative radiofrequency ablation. (a) The ablation is vaguely discernable in the B-mode image. Ablations boundaries are apparent in shear wave velocity (SWV) and maximum displacement (Max Disp) images in (b) and (c), respectively, and delineations were comparable among observers (s(SWV) = 0.96; s(Max Disp) = 0.90). Each color for the delineations in (b) and (c) represents a different observer. The gross pathology image in (d) shows that the ablation was formed in a region of the liver free from major inhomogeneities. Refer to Tables I and II, and IV for estimates of overlap with gross pathology, interobserver variability, and absolute and relative differences between elastographic imaging and gross pathology, respectively.

three observers on a particular shear wave velocity image). The Dice's coefficient (s), a similarity measure,[33] was used to investigate radiological-pathological variability and interobserver variability and is given by

$$s = \frac{2J}{1 + J}. \tag{3}$$

Representative examples of good and poor agreement between elastographic imaging and gross pathology are qualitatively presented in Figs. 1 and 2, and 6.

III. RESULTS

Shear wave velocity and maximum displacement images generated using EVE were similar to those previously reported.[28] Good lateral boundaries were observed, but some ambiguity was present above and below the ablation zone. The appearance of the ablation interior in both shear wave velocity and maximum displacement images was also influenced by inhomogeneities such as fissures and blood vessels. Figure 1 shows a representative RF ablation. Agreement among observers was high, with Dice's coefficients for shear wave velocity and maximum displacement images of 0.96 and 0.90, respectively. Lateral and axial boundaries were detected
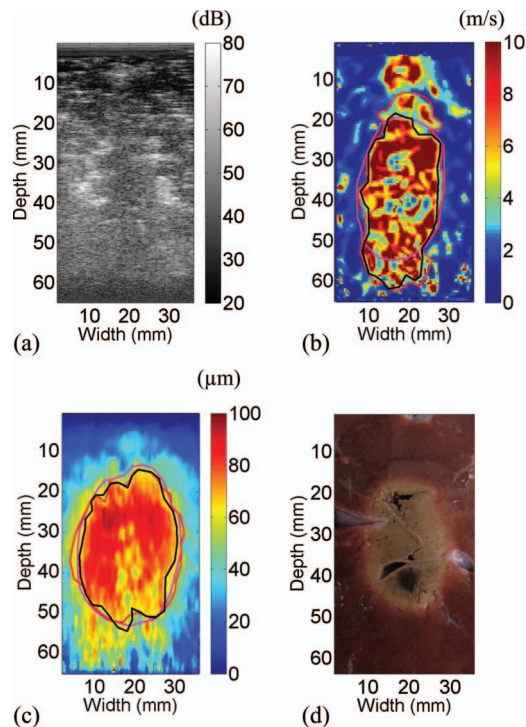
FIG. 2. Representative microwave ablation. Gas bubbles from the ablation procedure vaguely delineate the ablation in the B-mode image in (a). The shape and extent of the ablation on (b) shear wave velocity and (c) maximum displacement images are similar to (d) gross pathology. Each color for the delineations in (b) and (c) represents a different observer. Refer to Tables I and II, and IV for estimates of overlap with gross pathology, interobserver variability, and absolute and relative differences between elastographic imaging and gross pathology, respectively.

consistently by all three observers for shear wave velocity, maximum displacement, and gross pathology images. A representative MW ablation is shown in Fig. 2. Average Dice's coefficients for overlap between elastographic images and gross pathology and interobserver variability are presented in Tables I and II, respectively, and were similar for RF and MW ablations.

A comparison of thermal ablation areas on elastographic imaging and gross pathology is presented in Fig. 3. Elastographic imaging and gross pathology area estimates correlated better in RF than in MW ablations, as listed in Table III. Pearson coefficients were 0.79, 0.90, and 0.85 for RF ablations versus 0.54, 0.70, and 0.80 for MW ablations for shear wave velocity, maximum displacement, and combined images, respectively. The mean relative differences be-

tween RF and MW ablation areas and gross pathology area, as listed in Table IV, were 18.9% and 22.9% for shear wave velocity images, 16.0% and 23.1% for maximum displacement images, and 21.2% and 19.6% for combined images, respectively.

Investigation of ablation dimensions revealed further differences between elastographic imaging and gross pathology in RF and MW ablations. Short axis estimates for elastographic imaging and gross pathology are presented in Fig. 4. For both RF and MW ablations, short axis estimates from maximum displacement images correlated more closely to gross pathology than short axis estimates from shear wave velocity images. The mean relative difference between elastographic imaging and gross pathology for RF and MW ablations was 18.6% and 16.3% on shear wave velocity images, 8.7% and 14.2% on maximum displacement images, and 19.7% and 17.5% on combined images, respectively, as listed in Table IV. A comparison of long axis length estimates is presented in Fig. 5. Long axis estimates were more variable among observers on shear wave velocity images than on maximum displacement images.

A series of images showing an ablation with inconsistencies between elastographic imaging and gross pathology is shown in Fig. 6. Shear wave velocity and maximum displacement images indicate a much longer ablation than delineated on gross pathology. However, white arrows indicate a region on gross pathology in Fig. 6(d) that may have been treated. The black arrow indicates a blood vessel, which presents as an artifact in the shear wave velocity image.

IV. DISCUSSION

In this study, we investigated the feasibility of using EVE to visualize thermal ablation zones and sought to understand differences in RF and MW ablation visualization. Ablation dimensions on elastographic imaging and gross pathology were correlated, elastographic imaging and gross pathology similarity was estimated, and interobserver variability was quantified. Correlation statistics demonstrated a correspondence between elastographic imaging and gross pathology, and similarity measures showed that observers delineated ablations comparably. Artifacts influenced ablation representation on elastographic images. This study has provided further understanding of the representation and observer interpretation of RF and MW ablated regions on elastographic images created using EVE.

TABLE I. Elastographic imaging overlap with gross pathology.

	Radiofrequency			Microwave		
	Mean Dice's coefficient	Minimum Dice's coefficient	Maximum Dice's coefficient	Mean Dice's coefficient	Minimum Dice's coefficient	Maximum Dice's coefficient
SWV	0.71 ± 0.09	0.54	0.82	0.74 ± 0.09	0.52	0.86
Max Disp	0.81 ± 0.09	0.61	0.93	0.77 ± 0.12	0.47	0.90
Combined	0.76 ± 0.08	0.62	0.87	0.77 ± 0.10	0.59	0.89

Note: Average overlap is presented as mean ± standard deviation. Abbreviations are as follows: SWV = shear wave velocity, Max Disp = maximum displacement.

TABLE II. Interobserver variability.

	Radiofrequency			Microwave		
	Mean Dice's coefficient	Minimum Dice's coefficient	Maximum Dice's coefficient	Mean Dice's coefficient	Minimum Dice's coefficient	Maximum Dice's coefficient
SWV	0.83 ± 0.07	0.71	0.96	0.77 ± 0.08	0.62	0.86
Max Disp	0.86 ± 0.05	0.75	0.93	0.81 ± 0.09	0.64	0.90
Combined	0.76 ± 0.05	0.69	0.84	0.78 ± 0.11	0.44	0.89

Note: Mean Dice's coefficient is presented as mean ± standard deviation. Abbreviations are as follows: SWV = shear wave velocity, Max Disp = maximum displacement.

Observers were asked to delineate RF and MW ablations using elastographic images. Shear wave velocity images provide a measure of material stiffness, given that the material is nearly incompressible and isotropic. If these conditions are met, then the shear wave velocity is proportional to the Young's Modulus of a material. Soft tissue is primarily composed of water, making incompressibility a valid assumption. Isotropy is violated in the case of thermally ablated regions, as tissue density and stiffness change relative to untreated tissue following ablation.[34] In addition, wave reflections can affect wave speed estimation.[35,36] This may make stiffness estimation of thermal ablations with shear wave imaging qualitative, as with strain imaging. The maximum displacement images show the maximum shear wave displacement, which is greatest at the perturbation source (i.e., the electrode) and decays as the wave propagates through the tissue. Our observations show that the wave decays slowly within the ablated region and more rapidly in untreated tissue, which may result from

changing tissue properties caused by protein denaturation, tissue dehydration, and stiffness increases associated with thermal ablation.[28] In addition, wave reflections can cause a substantial decrease in wave amplitude as the wave travels from a stiff medium (i.e., the ablation) to a softer one (i.e., the untreated tissue).[37]

Ablation dimensions estimated from elastographic imaging and gross pathology were correlated, but correlations were lower than prior studies using elastic modulus imaging (EMI) on RF ablations[24] and SSI on HIFU ablations.[25] In the case of EMI, Jiang et al. determined Pearson coefficients of 0.85 and 0.95 for strain imaging and EMI area estimates, respectively. As listed in Table III, we obtained correlation coefficients of 0.79, 0.90, and 0.85 for RF ablations and 0.54, 0.70, and 0.80 for MW ablations for shear wave velocity, maximum displacement, and combined images, respectively. Short and long axis correlations were also lower, as listed in Table III. The lower correlation that we obtained may result from
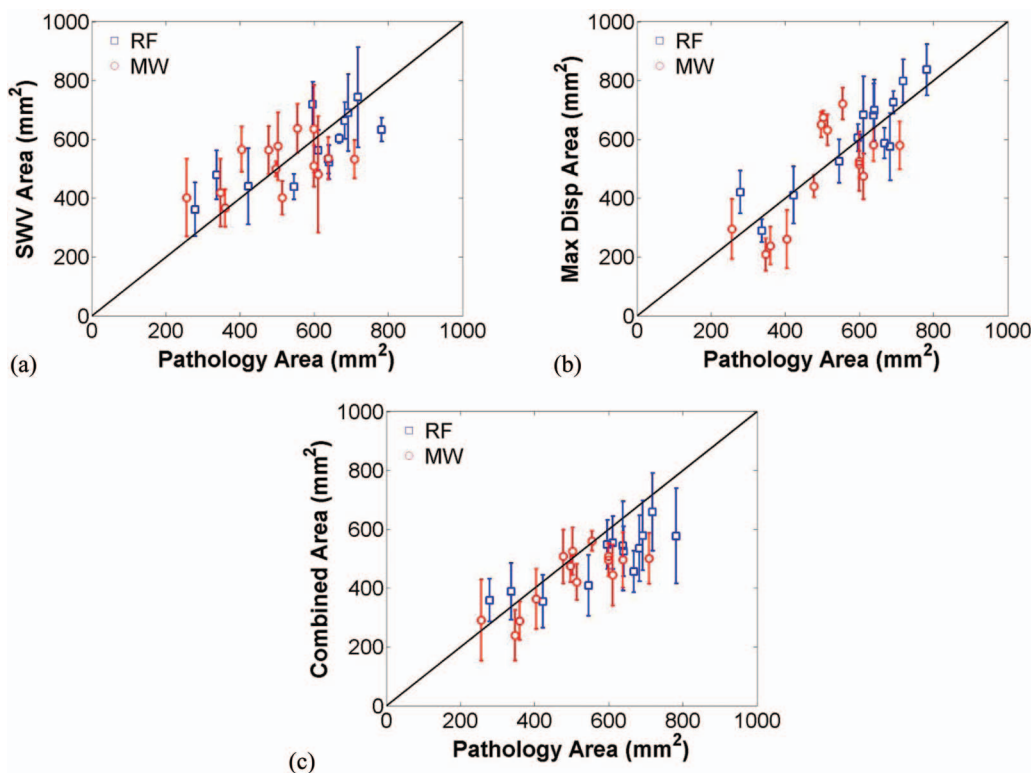

FIG. 3. Comparison of area estimates from shear wave velocity or maximum displacement to gross pathology for RF and MW ablations. Analysis of ablation area from (a) shear wave velocity images, (b) maximum displacement images, and (c) a combination of both images. Better correlation was observed between elastographic imaging and gross pathology for RF ablations, as listed in Table III.

TABLE III. Correlation coefficients for different ablation morphology measurements.

	Radiofrequency ($n = 13$)								
	Shear wave velocity			Maximum displacement			Combined		
	Area	SA	LA	Area	SA	LA	Area	SA	LA
Coefficient	0.79	0.67	0.78	0.90	0.87	0.57	0.85	0.78	0.48
R^2	0.62	0.45	0.61	0.81	0.76	0.32	0.73	0.60	0.23
p	0.0014	0.0115	0.0017	0.0001	<0.0001	0.0426	0.0002	0.0018	0.0998
	Microwave ($n = 14$)								
	Shear wave velocity			Maximum displacement			Combined		
	Area	SA	LA	Area	SA	LA	Area	SA	LA
Coefficient	0.54	0.44	0.69	0.70	0.60	0.67	0.80	0.69	0.74
R^2	0.29	0.19	0.47	0.49	0.36	0.45	0.64	0.47	0.54
p	0.0462	0.1196	0.0068	0.0054	0.0245	0.0090	0.0006	0.0065	0.0027
	All thermal ablations ($n = 27$)								
	Shear wave velocity			Maximum displacement			Combined		
	Area	SA	LA	Area	SA	LA	Area	SA	LA
Coefficient	0.71	0.61	0.72	0.81	0.75	0.65	0.84	0.74	0.65
R^2	0.51	0.37	0.52	0.66	0.56	0.43	0.70	0.55	0.42
p	<0.0001	0.0008	<0.0001	<0.0001	<0.0001	0.0002	<0.0001	<0.0001	0.0002

Note: Abbreviations are as follows: SA = short axis, LA = long axis.

TABLE IV. Summary of measurement differences between elastographic imaging and gross pathology.

		Radiofrequency					
		Mean difference		Minimum difference		Maximum difference	
		Absolute (mm^2 or mm)	Relative (%)	Absolute (mm^2 or mm)	Relative (%)	Absolute (mm^2 or mm)	Relative (%)
SWV	Area	100.6 ± 30.9	18.9 ± 9.2	41.1	6.0	148.7	42.2
	SA	4.5 ± 2.6	18.6 ± 9.5	0.7	3.5	8.0	31.6
	LA	3.7 ± 2.3	12.2 ± 7.6	1.4	4.3	9.1	29.3
Max Disp	Area	82.8 ± 34.8	16.0 ± 12.1	34.2	5.0	147.0	53.7
	SA	2.0 ± 0.9	8.7 ± 3.5	2.0	5.3	3.7	15.9
	LA	3.6 ± 1.8	11.9 ± 6.6	1.2	6.4	3.7	26.5
Comb	Area	120.8 ± 45.8	21.2 ± 6.6	67.6	12.8	211.4	31.7
	SA	4.7 ± 2.1	19.7 ± 7.5	1.2	6.4	7.3	28.6
	LA	3.4 ± 1.9	11.0 ± 5.7	0.7	2.3	7.4	21.0
		Microwave					
		Mean difference		Minimum difference		Maximum difference	
		Absolute (mm^2 or mm)	Relative (%)	Absolute (mm^2 or mm)	Relative (%)	Absolute (mm^2 or mm)	Relative (%)
SWV	Area	110.9 ± 49.6	22.9 ± 13.5	18.0	3.6	191.4	57.1
	SA	3.5 ± 1.8	16.3 ± 7.8	0.7	3.6	6.3	26.3
	LA	4.8 ± 3.0	17.0 ± 11.1	0.8	2.7	9.2	31.1
Max Disp	Area	112.8 ± 43.5	23.1 ± 10.0	36.9	7.7	172.3	35.5
	SA	2.9 ± 2.1	14.2 ± 10.6	0.9	4.4	8.0	40.5
	LA	4.4 ± 1.7	15.1 ± 5.9	1.6	5.0	6.9	24.9
Comb	Area	98.4 ± 49.1	19.6 ± 9.4	27.5	5.0	207.7	41.6
	SA	3.7 ± 1.7	17.5 ± 7.8	1.0	4.4	6.2	31.7
	LA	2.9 ± 0.6	10.4 ± 6.9	0.6	1.7	6.1	25.4

Note: Mean differences vare presented as mean ± standard deviation. Abbreviations are as follows: SWV = shear wave velocity, Max Disp = maximum displacement, Comb = combined, SA = short axis, LA = long axis.
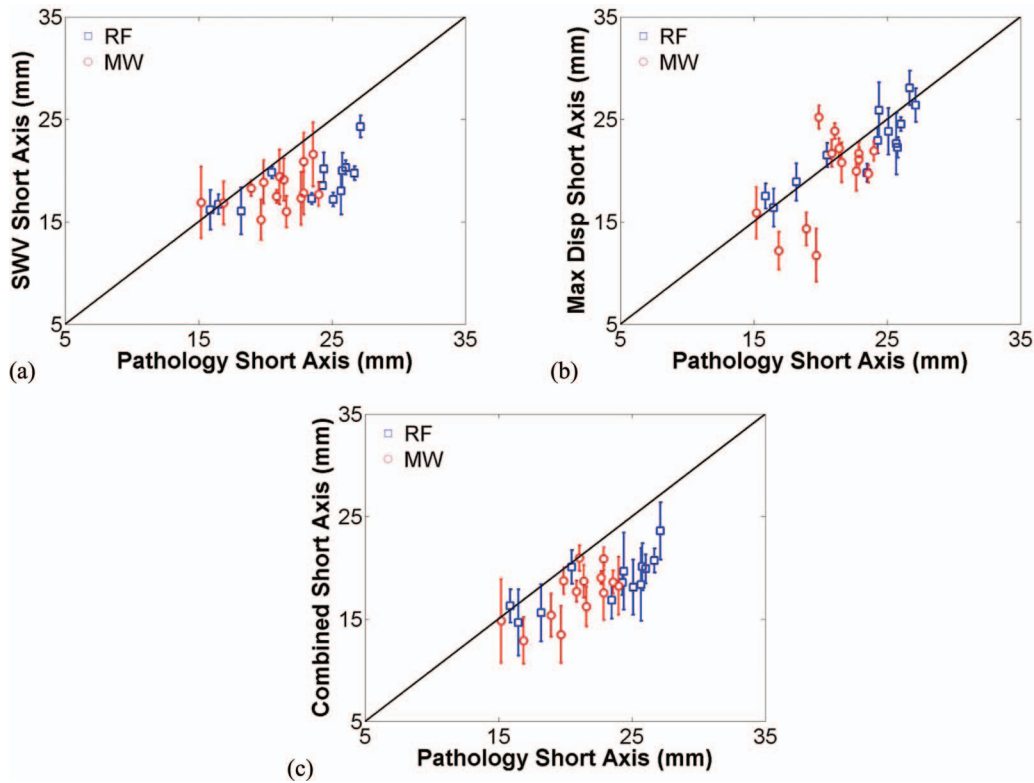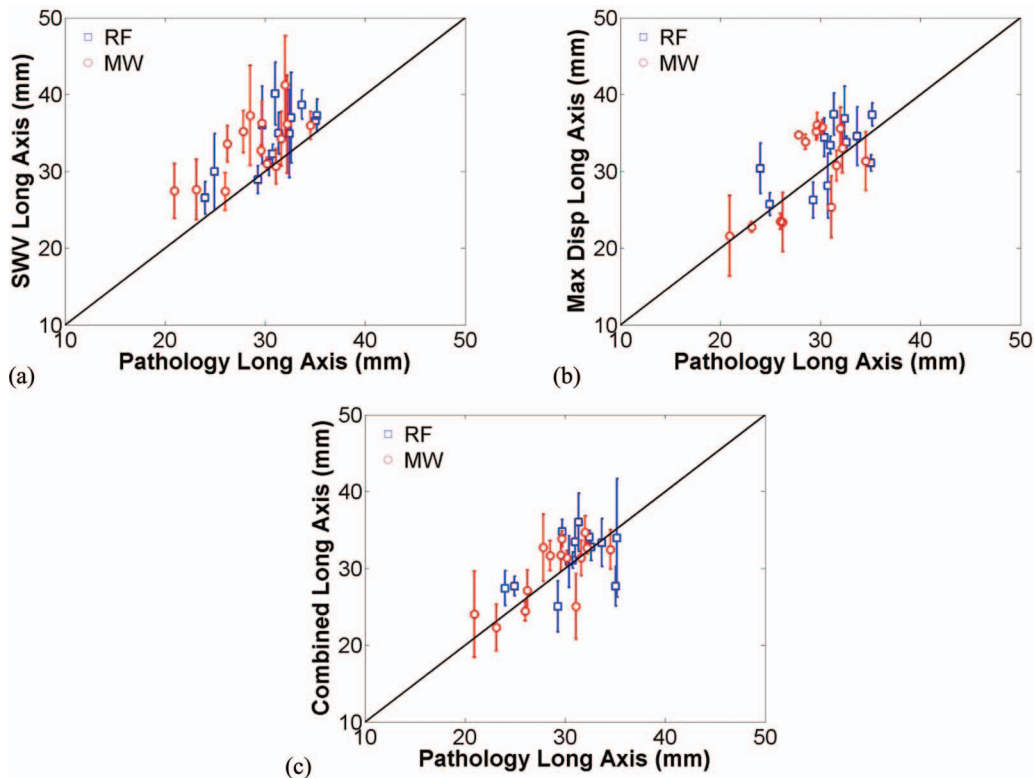
FIG. 4. Comparison of short axis length estimates from shear wave velocity or maximum displacement images when compared to gross pathology for RF and MW ablations. Shear wave velocity images tended to underestimate gross pathology short axis length in (a) with increasing short axis length. The discrepancy between maximum displacement and gross pathology was less in (b). The trend in (c) using a combination of shear wave velocity and maximum displacement images is similar to (a), using only shear wave velocity images.

FIG. 5. Comparison of long axis length estimates from shear wave velocity or maximum displacement images when compared to gross pathology for RF and MW ablations. Shear wave velocity images tended to overestimate long axis length compared to gross pathology in (a). This discrepancy was lower using maximum displacement images or a combination of shear wave velocity and maximum displacement images in (b) and (c).
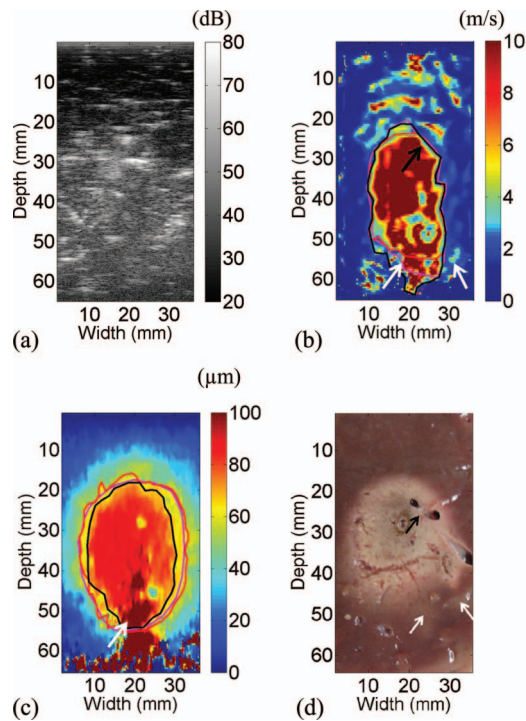
FIG. 6. Radiofrequency ablation with overlap discrepancies on shear wave velocity or maximum displacement images. The B-mode image in (a) vaguely shows the ablation location. Shear wave velocity (b) and maximum displacement (c) images apparently overestimate the ablation length determined from gross pathology (d). However, the white arrows in (d) indicate a region that appears to be treated, which was delineated in both (b) and (c). The black arrow highlights a blood vessel, which is represented as a region of low shear wave velocity in (b). Each color for the delineations in (b) and (c) represents a different observer. Refer to Tables I and II, and IV for estimates of overlap with gross pathology, interobserver variability, and absolute and relative differences between elastographic imaging and gross pathology, respectively.

artifacts in the images that can be caused by blood vessels or fissures within the ablation, wave reflections, or the ablation needle itself. In the case of SSI, the correlation was 0.95 for 5 HIFU ablations.[25] However, these ablations were formed in chicken muscle, the method of energy deposition was different (HIFU vs RF or MW), and the ablation sizes did not overlap with the present study (∼5–10 mm wide vs ∼15–30 mm wide), making direct comparison impractical.

Area estimated from shear wave velocity or combined images trended towards underestimating gross pathology as ablation size increased, as shown in Fig. 3. This is consistent with a prior study using external compression elastography.[38] An explanation for this observation may be the energy deposition method. For smaller ablations, the energy deposition is more homogenous. As the ablation size grows, energy deposition is more diffuse on the ablation perimeter, resulting in a softer ablation periphery. This phenomenon has been quantified via dynamic indentation[34] and may explain increases in area underestimation with increasing ablation size. The dynamic range of the image may alter ablation appearance because of the large difference in stiffness between the ablation center and periphery. Logarithmic or power-law compression may also provide better visualization. In this study, ablations were not delineated with a compressed shear wave velocity

scale, but this may be beneficial for future studies. Wave reflections may also play a role. However, in our previous work in homogenous phantoms, reflections caused high shear wave velocity artifacts on the inclusion periphery but no change in the inclusion area.[28]

We investigated ablation representation further by estimating short and long axis lengths in all images. As shown in Figs. 4 and 5, on elastographic images, the short axis typically underestimated the short axis on gross pathology, whereas the long axis typically overestimated the long axis on gross pathology. As with area, short axis underestimation on shear wave velocity images was worse for larger ablations, which may indicate a softer periphery resulting from decreased energy deposition. The overestimation of the long axis length on shear wave velocity images is likely the result of artifacts above and below the ablation.[28] This is corroborated by the variability of the long axis estimates, which was much greater than that of the short axis (i.e., lateral boundaries) estimates. Absolute differences for short and long axis estimates were under 5 mm, or 2.5 mm margins, which is smaller than the minimum acceptable margin of 4 mm often used clinically.[39] In a future study, the ablation boundary may be more accurately estimated on gross pathology by performing EVE in an *in vivo* model and staining ablated volumes for cell viability to evaluate cell death.[34] However, EVE as described is prone to motion artifacts because of the sequential scanning employed.[28] Plane wave insonification and a parallel-receive device would sufficiently increase the acquisition speed to perform *in vivo* experiments.[40]

Hepatic blood vessels influenced ablation representation on shear wave velocity images. As shown in Fig. 6(b), the low shear wave velocity artifact produced by the blood vessel decreased the apparent extent of the ablation. However, the observers did delineate the region with the blood vessel in the maximum displacement image in this particular example. Another interesting observation is that both shear wave velocity and maximum displacement delineations include a stiff region below the observer delineations on gross pathology. There is a subtle lightened color below the ablation delineations in Fig. 6(d) indicated by the white arrows, which may be a region that was treated by hot gases escaping the ablation core through blood vessels.

In this study, we have investigated RF and MW ablations as represented on shear wave velocity and maximum displacement images created using EVE. Lateral margins were more consistently delineated than axial margins because of artifacts present above and below the thermal ablations. Area underestimation was consistent with prior studies, and it may be the result of either low mechanical contrast or wave reflections on the ablation periphery. Observers also delineated lesion boundaries comparably. Although EVE in its current form has limitations, understanding ablation representation on shear wave velocity and maximum displacement images will lead to improvements in the technique. Future developments to EVE may improve physician confidence during ablation procedures, increasing the likelihood of complete treatment, lowering the rate of tumor recurrence, and potentially leading to new applications of thermal ablation therapy.

ACKNOWLEDGMENTS

[a] Authors to whom correspondence should be addressed. Electronic Addresses: dewall@wisc.edu and tvarghese@wisc.edu; Telephone: (616) 405-9172; Fax: (608) 262-2413.

[1] J. Bruix, M. Sherman, J. M. Llovet, M. Beaugrand, R. Lencioni, A. K. Burroughs, E. Christensen, L. Pagliaro, M. Colombo, and J. Rodes, "Clinical management of hepatocellular carcinoma. Conclusions of the Barcelona-2000 EASL conference. European association for the study of the liver," J. Hepatol. **35**, 421–430 (2001).

[2] H. Bismuth and P. E. Majno, "Hepatobiliary surgery," J. Hepatol. **32**, 208–224 (2000).

[3] P. F. Laeseke, T. M. Frey, C. L. Brace, L. A. Sampson, T. C. Winter III, J. R. Ketzler, and F. T. Lee, Jr., "Multiple-electrode radiofrequency ablation of hepatic malignancies: Initial clinical experience," AJR, Am. J. Roentgenol. **188**, 1485–1494 (2007).

[4] M. D. Lu, H. X. Xu, X. Y. Xie, X. Y. Yin, J. W. Chen, J. Kuang, Z. F. Xu, G. J. Liu, and Y. L. Zheng, "Percutaneous microwave and radiofrequency ablation for hepatocellular carcinoma: A retrospective comparative study," J. Gastroenterol. **40**, 1054–1060 (2005).

[5] M. Sato, Y. Watanabe, S. Ueda, S. Iseki, Y. Abe, N. Sato, S. Kimura, K. Okubo, and M. Onji, "Microwave coagulation therapy for hepatocellular carcinoma," Gastroenterology **110**, 1507–1514 (1996).

[6] R. J. Zagoria, J. A. Pettus, M. Rogers, D. M. Werle, D. Childs, and J. R. Leyendecker, "Long-term outcomes after percutaneous radiofrequency ablation for renal cell carcinoma," Urology **77**, 1393–1397 (2011).

[7] P. F. Laeseke, F. T. Lee, Jr., L. A. Sampson, D. W. van der Weide, and C. L. Brace, "Microwave ablation versus radiofrequency ablation in the kidney: High-power triaxial antennas create larger ablation zones than similarly sized internally cooled electrodes," J. Vasc. Interv. Radiol. **20**, 1224–1229 (2009).

[8] K. Steinke, "Radiofrequency ablation of pulmonary tumours: Current status," Cancer Imaging **8**, 27–35 (2008).

[9] S. C. Rose, P. A. Thistlethwaite, P. E. Sewell, and R. B. Vance, "Lung cancer and radiofrequency ablation," J. Vasc. Interv. Radiol. **17**, 927–951 (2006).

[10] M. R. Callstrom and J. W. Charboneau, "Percutaneous ablation: Safe, effective treatment of bone tumors," Oncology (Williston Park) **19**, 22–26 (2005).

[11] Z. W. Peng, Y. J. Zhang, M. S. Chen, H. H. Liang, J. Q. Li, Y. Q. Zhang, and W. Y. Lau, "Risk factors of survival after percutaneous radiofrequency ablation of hepatocellular carcinoma," Surg. Oncol. **17**, 23–31 (2008).

[12] G. S. Gazelle, S. N. Goldberg, L. Solbiati, and T. Livraghi, "Tumor ablation with radio-frequency energy," Radiology **217**, 633–646 (2000).

[13] S. N. Goldberg, G. S. Gazelle, and P. R. Mueller, "Thermal ablation therapy for focal malignancy: A unified approach to underlying principles, techniques, and diagnostic imaging guidance," AJR, Am. J. Roentgenol. **174**, 323–331 (2000).

[14] D. E. Malone, L. Lesiuk, A. P. Brady, D. R. Wyman, and B. C. Wilson, "Hepatic interstitial laser photocoagulation: Demonstration and possible clinical importance of intravascular gas," Radiology **193**, 233–237 (1994).

[15] S. N. Goldberg, G. S. Gazelle, C. C. Compton, P. R. Mueller, and K. K. Tanabe, "Treatment of intrahepatic malignancy with radiofrequency ablation: Radiologic-pathologic correlation," Cancer **88**, 2452–2463 (2000).

[16] T. Wu, J. P. Felmlee, J. F. Greenleaf, S. J. Riederer, and R. L. Ehman, "Assessment of thermal tissue ablation with MR elastography," Magn. Reson. Med. **45**, 80–87 (2001).

[17] Y. C. Fung, *Biomechanics: Mechanical Properties of Living Tissues* (Springer, New York, 1993).

[18] R. J. Dewall, S. Bharat, T. Varghese, M. E. Hanson, R. M. Agni, and M. A. Kliewer, "Characterizing the compression-dependent viscoelastic properties of human hepatic pathologies using dynamic compression testing," Phys. Med. Biol. **57**, 2273–2286 (2012).

[19] M. Zhang, B. Castaneda, J. Christensen, W. Saad, K. Bylund, K. Hoyt, J. G. Strang, D. J. Rubens, and K. J. Parker, "Real-time sonoelastography of hepatic thermal lesions in a swine model," Med. Phys. **35**, 4132–4141 (2008).

[20] S. Bharat, T. Varghese, E. L. Madsen, and J. A. Zagzebski, "Radiofrequency ablation electrode displacement elastography: A phantom study," Med. Phys. **35**, 2432–2442 (2008).

[21] N. Rubert, S. Bharat, R. J. DeWall, A. Andreano, C. Brace, J. Jiang, L. Sampson, and T. Varghese, "Electrode displacement strain imaging of thermally-ablated liver tissue in an in vivo animal model," Med. Phys. **37**, 1075–1082 (2010).

[22] S. Bharat and T. Varghese, "Contrast-transfer improvement for electrode displacement elastography," Phys. Med. Biol. **51**, 6403–6418 (2006).

[23] B. J. Fahey, R. C. Nelson, S. J. Hsu, D. P. Bradway, D. M. Dumont, and G. E. Trahey, "In vivo guidance and assessment of liver radio-frequency ablation with acoustic radiation force elastography," Ultrasound Med. Biol. **34**, 1590–1603 (2008).

[24] J. Jiang, C. Brace, A. Andreano, R. J. DeWall, N. Rubert, T. G. Fisher, T. Varghese, F. Lee, Jr., and T. J. Hall, "Ultrasound-based relative elastic modulus imaging for visualizing thermal ablation zones in a porcine model," Phys. Med. Biol. **55**, 2281–2306 (2010).

[25] B. Arnal, M. Pernot, and M. Tanter, "Monitoring of thermal therapy based on shear modulus changes: II. Shear wave imaging of thermal lesions," IEEE Trans. Ultrason. Ferroelectr. Freq. Control **58**, 1603–1611 (2011).

[26] B. Arnal, M. Pernot, and M. Tanter, "Monitoring of thermal therapy based on shear modulus changes: I. Shear wave thermometry," IEEE Trans. Ultrason. Ferroelectr. Freq. Control **58**, 369–378 (2011).

[27] M. Orescanin, M. A. Qayyum, K. S. Toohey, and M. F. Insana, "Dispersion and shear modulus measurements of porcine liver," Ultrason. Imaging **32**, 255–266 (2010).

[28] R. J. Dewall, T. Varghese, and E. L. Madsen, "Shear wave velocity imaging using transient electrode perturbation: Phantom and ex vivo validation," IEEE Trans. Med. Imaging **30**, 666–678 (2011).

[29] C. L. Brace, "Microwave tissue ablation: Biophysics, technology, and applications," Crit. Rev. Biomed. Eng. **38**, 65–78 (2010).

[30] J. Bercoff, M. Tanter, and M. Fink, "Supersonic shear imaging: a new technique for soft tissue elasticity mapping," IEEE Trans. Ultrason. Ferroelectr. Freq. Control **51**, 396–409 (2004).

[31] M. L. Palmeri, M. H. Wang, J. J. Dahl, K. D. Frinkley, and K. R. Nightingale, "Quantifying hepatic shear modulus in vivo using acoustic radiation force," Ultrasound Med. Biol. **34**, 546–558 (2008).

[32] R. J. DeWall and T. Varghese, "Improving thermal ablation delineation with electrode vibration elastography using a bidirectional wave propagation assumption," IEEE Trans. Ultrason. Ferroelectr. Freq. Control **59**, 168–173 (2012).

[33] A. P. Zijdenbos, B. M. Dawant, R. A. Margolin, and A. C. Palmer, "Morphometric analysis of white matter lesions in MR images: Method and validation," IEEE Trans. Med. Imaging **13**, 716–724 (1994).

[34] R. J. DeWall, T. Varghese, and C. L. Brace, "Quantifying local stiffness variations in radiofrequency ablations with dynamic indentation," IEEE Trans. Biomed. Eng. **59**, 728–735 (2012).

[35] M. L. Palmeri, N. C. Rouze, M. H. Wang, D. Xuan, and K. R. Nightingale, "Quantifying the impact of shear wavelength and kernel size on shear wave speed estimation," Proc.-IEEE Ultrason. Symp. (San Diego, CA, 2010), pp. 13–16.

[36] T. Deffieux, J. L. Gennisson, J. Bercoff, and M. Tanter, "On the effects of reflected waves in transient shear wave elastography," IEEE Trans. Ultrason. Ferroelectr. Freq. Control **58**, 2032–2035 (2011).

[37] M. L. Palmeri, S. A. McAleavey, K. L. Fong, G. E. Trahey, and K. R. Nightingale, "Dynamic mechanical response of elastic spherical inclusions to impulsive acoustic radiation force excitation," IEEE Trans. Ultrason. Ferroelectr. Freq. Control **53**, 2065–2079 (2006).

[38] T. Varghese, U. Techavipoo, W. Liu, J. A. Zagzebski, Q. Chen, G. Frank, and F. T. Lee, Jr., "Elastographic measurement of the area and volume of thermal lesions resulting from radiofrequency ablation: Pathologic correlation," AJR, Am. J. Roentgenol. **181**, 701–707 (2003).

[39] C. H. Liu, R. S. Arellano, R. N. Uppot, A. E. Samir, D. A. Gervais, and P. R. Mueller, "Radiofrequency ablation of hepatic tumours: Effect of postablation margin on local tumour progression," Eur. Radiol. **20**, 877–885 (2010).

[40] L. Sandrin, M. Tanter, S. Catheline, and M. Fink, "Shear modulus imaging with 2-D transient elastography," IEEE Trans. Ultrason. Ferroelectr. Freq. Control **49**, 426–435 (2002).